Cost Effective MIL-53(Cr) Metal-Organic Framework Based Supercapacitors Encompassing Fast-Ion (Li⁺/H⁺/Na⁺) Conductors

Manoranjan Ojha,[a] Billy Wu,[b] Melepurath Deepa[a,]*

[a]*Department of Chemistry, Indian Institute of Technology Hyderabad, Kandi, Sangareddy-502285, Telangana (India)*

[b]*Dyson School of Design Engineering, Imperial College, London. SW7 2AZ (United Kingdom)*

ABSTRACT: Chromium based low cost metal-organic framework (MOF) cathode (MIL (Matériaux de l'Institut Lavoisier)-53(Cr)), is coupled with a bio-source derived porous carbon (BPC) anode, produced from abundantly available agricultural waste betel nut shells in an asymmetric supercapacitor, for the first time. The impact of the electrolyte on the electrochemical behavior of an asymmetric BPC//MIL-53(Cr) supercapacitor was assessed by constructing cells with the following electrolytes: proton conducting camphorsulfonic acid (CSA), Li⁺ ion conducting- solutions of LiClO₄, Na⁺ ion conducting sodium poly(4-styrene sulfonate) (NaPSS) solution and ionic liquid (IL:1-butyl-1-methyl-pyrrolidinium trifluoromethanesulfonate) based solutions. The aqueous H⁺-ion based CSA electrolyte shows a superior ionic conductivity (270 S cm⁻¹), enhanced transport number (0.96), carries larger ionic currents, and retains high conductivity even at sub-ambient temperatures; clearly outperforming all the other Li⁺/Na⁺/IL–electrolytes. The BPC/aqueous CSA or LiClO₄/MIL-53(Cr) supercapacitors show enhanced storage performances, with the H⁺ cell having a specific capacitance of 70 F g⁻¹, energy and power density maxima of 9.7 Wh kg⁻¹ and 0.25 kW kg⁻¹ and endures 10⁴ cycles. A detailed account of the dependence of electrolyte cation/anion- and solvent- type on electrochemical charge storage provides a basis for adapting these design principles to developing high performance MOF based supercapacitors.

Keywords: Metal-organic frameworks, activated carbon, electrolyte, capacitance, supercapacitor

Introduction

Transition metal ion containing metal-organic frameworks (MOFs) are widely employed in energy storage devices like pseudocapacitors due to their ability to undergo facile Faradaic reactions, low processing cost, ease of synthesis, and their intrinsic property to adsorb, accommodate and release molecules into and from the highly ordered arrangement of pores[1-4]. However, one of the principal reasons why industry and academia are gravitating towards MOFs, is because the elementary units of the framework, metal ions and the organic linkers, can be combined in numerous ways to create new materials with tailored structures. Among MOFs, the most commonly used ones are the mono-metallic oxides of Co_3O_4[5-8] and Mn_xO_y[9,10], bimetallic: Zn/Co-[11,12] Zn/Ni-[13,14] and Ni/Co-[15-17] oxide based polyhedral structures or nanostructures, which are all derived directly or from the pyrolysis of their MOFs. However, these highly porous metal oxide networks obtained from MOFs are reactive and have a tendency to undergo uncontrolled redox reactions, which can either result in the collapse of their organized microstructure or manifest in phase changes, culminating in significant capacitance decay as a function of cycling[18]. Thus, there is a need to develop new synthesis methodologies that can produce robust, crystalline and porous metal oxide networks with high effective surface area. While homogeneous porosity allows rapid access of the electrolyte solution through the entity of an electrode, good crystallinity permits unrestricted deep penetration of electrolyte ions through the structural voids, thus maximizing the power and energy density. High effective surface area increases the area of contact between the MOF derived oxide and the electrolyte, which enhances the capacitance of the electrode[19].

Of the various MOFs for energy storage devices, chromium (Cr) based oxide networks are easy to fabricate and possess good chemical stability, however have not been extensively studied. MIL (Matériaux de l'Institut Lavoisier)-101(Cr), which is a Cr based MOF, has shown promising performance for diverse applications that include: (i) hydrogen storage [20,21] (ii) as an effective adsorbent for capture of gases like CO_2[22], CH_4[23], CO_2[24], H_2S[25] and (iii) as a catalytic support for metal nanoparticles in catalytic reactions[21]. Ren and co-workers successfully performed large scale, one-pot synthesis of MIL-101(Cr) with high reproducibility at low cost by direct use of waste poly(ethylene terephthalate) or PET as a source of terephthalic acid and used environmentally friendly formic acid as the modulator. They also simultaneously addressed the problem of recycling large amounts of PET waste. The PET-derived Cr-MOF products were found to have excellent textural properties with high hydrogen adsorption (storage) properties[21]. This MOF is known for its low density, high stability to moisture, thermal stability, unusually large pore volume and high effective surface area, and ample unsaturated active chromium sites.

To be economically viable on an industrial scale, large-scale manufacturing of Cr-MOF at an acceptable cost is an imminent requirement. To this end, here we report the synthesis of a chemically stable, redox active Cr-MOF called MIL-53(Cr) through a hydrothermal synthesis route from a suspension of cheaply and easily available terephthalic acid (TPA) and a chromium salt[26], followed by its application as a cathode in an asymmetric supercapacitor. The anode consists of a bioderived porous carbon (BPC) which uses

waste betel nut pods as the precursor combined with a chemical activation process.

Besides the usage of the Cr-MOF for the first time in an asymmetric supercapacitor (BPC//MIL-53(Cr)), this paper also focuses on understanding the effect of electrolyte cation and anion on the energy storage performance. The salient feature of the MIL-53 structure is the inorganic M-OH chains inter-linked via the organic terephthalate species, resulting in a framework having regularly spaced one-dimensional diamond-shaped pores which are conducive for ion-adsorption during cycling[26]. While there are a plethora of independent reports on the use of proton- (H_2SO_4)[27] hydroxyl ion- (KOH)[28], lithium ion- ($LiCF_3SO_3$)[29], sodium ion- ($NaClO_4$)[30], potassium ion- (K_2SO_4 or KCl)[31,32], ionic liquid cation or anion (1-ethyl-3-methyl-imidazolium bis(trifluoromethylsulfonyl)imide-[33,34] conducting liquid and gel electrolytes for supercapacitors, a consolidated study on the influence of electrolyte cation/anion on supercapacitor performance parameters remains elusive. As a rule of thumb, the broad criteria of high ionic conductivity (preferably > 10^{-3} S cm^{-1}), a wide electrochemical potential stability window (preferably > 1 V), broad thermal stability range from -10 ^{o}C to +60 ^{o}C or better, good chemical stability and low vapor pressure are typically taken into consideration for the electrolyte[35]. Since some, or occasionally many, of these criteria are met by the above-mentioned electrolytes, they are simply directly deployed in supercapacitors, without giving the required attention to the role of the electrolyte in controlling the cell performance. This study attempts to bridge this gap, and provides valuable insights on how the choice of an appropriate electrolyte is of paramount importance as it directly governs the cell performance in terms of specific capacitance (SC), energy density (E), power density (P) and equivalent series resistance (ESR), among others.

Given this background, a range of liquid electrolytes: (i) H$^+$ ion conducting aqueous camphorsulfonic acid (CSA) solution, Li$^+$ ion conducting- (ii) aqueous and (iii) non-aqueous solutions of $LiClO_4$ in water and propylene carbonate (PC), (iv) Na$^+$ ion conducting aqueous sodium poly(4-styrene sulfonate) (NaPSS) solution and (v) IL-ion conducting non-aqueous solution of 1-butyl-1-methyl-pyrrolidinium trifluoromethanesulfonate [BuMePy][CF$_3$SO$_3$] in PC were used in an asymmetric BPC//MIL-53(Cr) supercapacitor, and the influence of the electrolyte cation, anion and medium on cell properties are studied. Structural aspects of the individual active materials: Cr-MOF and BPC, and their redox activity also assisted in discerning the performance parameters of the full cells. The study concludes with how the low cost, non-toxic, and safe to use aqueous fast-ion conducting CSA electrolyte delivers an optimal performance compared to all the remaining electrolytes in terms of capacity retention with cycling, SC, safety, cost and due to the synergy between ionic mobility, conductivity, transport number, and its ability to form strong interfacial contact with the active electrodes. A succinct correlation between electrochemical energy storage behavior of a supercapacitor with the physicochemical and redox properties of liquid electrolytes

is presented and the outcomes of this work are anticipated to be of great significance for designing high performance MOF based supercapacitors.

Experimental

Chemicals

Chromium nitrate nonahydrate (Cr(NO$_3$)$_3$·9H$_2$O, 99%), ter-ephthalic acid (TPA, 98%), dimethyl sulfonxide (DMSO, 99%), (1S)- (+)-10-camphorsulphonic acid (CSA, 99%), poly(sodium 4-styrenesulfonate) (NaPSS, 98%), 1-butyl-1-methyl-pyrrolidinium trifluoromethanesulfonate ([BuMePy][CF$_3$SO$_3$], 98%), carbon black Super P (Timcal), ethanol (98%), lithium perchlorate (LiClO$_4$), poly(vinyli-dene fluoride) (PVdF, average M$_W$: 534000), N-methyl pyr-rolidone (NMP), were procured from Sigma-Aldrich and used as recieved. Ultrapure water (resistivity ~18.2 MΩ cm) was obtained through a Millipore Direct-Q3 UV system. Nickel (Ni) foam current collectors were procured from Gelon and used after cleaning them with acetone.

Synthesis of Cr-MOF

MIL-53(Cr) MOF was synthesized by using a previously re-ported method[26]. Chromium nitrate nonahydrate (1.6 g, 6.72 mmol) was dissolved in 50 mL of DMSO in a 100 mL beaker. To this clear blue colored solution, a solution (50 mL) of terephthalic acid (0.66 g, 3.97 mmol) in DMSO was added dropwise and magnetically stirred for 1 h at ambient temperature. The resulting solution was transferred to a 200 mL autoclave and heated for 12 h at 180 °C. A blue hy-drogel was obtained which was first washed with DMSO to remove the excess terephthalic acid and then washed with ethanol. The compound was dried at 60 °C in open air for 12 h and green translucent crystals with a glassy appearance were obtained. The compound was ground and heated at 200 °C for 24 h in a furnace. The cooled product was dark green in color, labelled as Cr-MOF or MIL-53(Cr) and kept in desiccator for further use. Scheme 1 shows the step-wise synthesis of the MOF.

Synthesis of bio-derived porous carbon (BPC)

BPC was synthesized from betel nuts shells as a biomass source. The shells were collected and washed several times with ultrapure water. The shells were cut into small pieces and transferred to an autoclave for heating at 70 °C for 12 h to char the sample in the presence of ultrapure water. The resulting brown-reddish colored sample was washed with ethanol and dried at 70 °C in open air. The dried sample was heated for 4 h to reach the final temperature 750 °C and at this temperature the heating was continued for another 4 h. The calcined carbon was ground and activated using aque-ous KOH (1:1 w/w) by using a minimum amount of water. The mixture was stirred at 80 °C for 12 h. The activated car-bon mixture was filtered and washed with ultrapure water several times until the pH of the filtrate was 7. Finally, the activated carbon was dried at 70 °C in open air and stored in desiccator. The formation of BPC is shown through pho-tographs in Scheme 1.

Cell fabrication

The Cr-MOF electrode (cathode) was prepared by dry grinding of Cr-MOF powder, BPC, carbon black (CB) and

PVdF in a weight ratio of 60:20:10:10. The mentioned compound mixture was well ground by using a mortar-pestle for 1 h. A few drops of NMP were added to the mixture and again ground for another 30 min. to get a consistent slurry. The prepared slurry was coated on the Ni foam over a geometrical area of 1 cm². The coated electrodes were dried in a vacuum oven at 70 °C for 12 h and kept in desiccator. In a similar way, the BPC electrode (anode) was prepared by mixing BPC, CB and PVdF in the weight ratio of 80:10:10. The weight of the active material at each of the two electrodes was calculated to be ~2 mg, and exact weights were used in the calculations. The mass loadings of two electrodes were balanced by using the equation: $m_-/m_+ = (C_+V_+)/(C_-V_-)$ and more details can be found in the supporting information (Figure S1). Asymmetric cells were fabricated in the following configuration: Ni foam-BPC//Cr-MOF-Ni foam in a sandwich manner with a Whatman filter paper (Cat. number 1001-125) serving as a separator between two electrodes. Three drops of the electrolyte solution (0.1 mL) were added on the filter paper before joining the electrodes and the cells were rested for 5 h, and the edges were sealed with an epoxy glue and dried in air before testing. A representative full cell is illustrated in Scheme 1.

Instrumentation techniques

X-ray diffraction patterns were recorded on a PANalytical, X'PertPRO instrument with a Cu-Kα (λ = 1.5406 Å) radiation X-ray source. Surface morphology analysis was carried out on a field emission scanning electron microscope (FE-SEM, JEOL-JSM-7800). Transmission electron microscopy (TEM) images were obtained on a JEOL 2100 microscope operating at an accelerating voltage of 200 kV by using specimens coated over carbon coated copper grids by employing the suspension and evaporation technique. Brunauer-Emmett-Teller (BET) surface area- and Barrett-Joyner-Halenda (BJH) pore size- analysis were carried for Cr-MOF and BPC under an inert nitrogen atmosphere at ~77 K, after degassing was done at 300 °C for 6 h. X-ray photoelectron spectroscopy (XPS) measurements were performed on an ESCALAB 250Xi instrument, working at a base pressure of ~6×10^{-11} Torr having a non-monochromatized Al Kα line at 1486.7 eV. The acquired resolution of survey and core levels were 1 and 0.1 eV and the spectra were acquired at 200 and 50 eV pass energies respectively. The core-level spectra were deconvoluted using a non-linear iterative least-squares Gaussian fitting procedure. Corrections due to charging effects were accounted for by using C(1s) as an internal reference and the Fermi edge of a gold sample. A Jandel Peak FitTM (version 4.01) program was used for the analysis. Galvanostatic charge-discharge (GCD), cyclic voltammetry (CV), linear sweep voltammetry (LSV), chronoamperometry studies were performed on an Autolab PGSTAT 204 potentiostat-galvanostat and the electrochemical impedance spectroscopic (EIS) studies were performed on an Autolab PGSTAT 302 frequency response analyzer.

Results and discussion

Structural features of MIL-53(Cr) and BPC

Raman spectra of Cr-MOF and MIL-53(Cr) (Figure 1a) shows multiple strong features with the peak at 867 cm⁻¹, which is attributed to the (C-H) deformation vibration, and matches reasonably well with an absorption band at 880 cm⁻¹ obtained for MIL-101(Cr)[24]. This is followed by a peak at 962 cm⁻¹ which originates from the bending vibrational mode [δ(C-O-H)] of the carboxylate groups on terephthalic acid[36] and the band at 1144 cm⁻¹, is ascribed to the [δ(Cr-O-H)] bending vibrations typical of hydroxyl bridged complexes, based on a similar peak assignment made for gray colored chromium terephthalate[37]. Subsequent bands at 1440 and 1609 cm⁻¹ are attributed to the stretching vibration of C=C bonds on the aromatic benzene moiety[24] and the C=O stretching vibration of the -COO groups on terephthalic acid[37]. The latter band's position is strongly governed by the chemical environment of the carboxylate ions. Ionic and coordinated terephthalates appear at lower frequencies compared to the covalent terephthalic acid, which produces this band at 1690 cm⁻¹[37]. The low intensity peak observed at ~633 cm⁻¹, corresponds to a lattice Cr-O vibration, in line with a previous assignment at ~640 cm⁻¹, made for chromium oxide at 640 cm⁻¹[38]. The XRD pattern of the Cr-MOF shows peaks at 2θ = 9.3°, 18.2°, 25.3° and 43.3°, corresponding to inter-planar spacings (d) of 9.5, 4.87, 3.43 and 2.08 Å (Figure 1b). These peaks match well with those reported for MIL-53as and Cr^{III}-(OH){OOC-C₆H₄-COO}₂{HOOC-C₆H₄-COOH}$_{0.75}$, with an orthorhombic structure and lattice parameters: a, b and c of 17.34, 12.178 and 6.822 Å[26]. The structure, as shown through Figure 1c, is composed of corner sharing Cr-octahedra connected through the (OH) bridging groups. The chains are linked together with dicarboxylates creating the 3D-nanoporous structure. The anions of Cr-octahedra are two-OH groups in trans-positions and four oxygens that stem from the dicarboxylates. The presence of free terephthalic acid in the pores is also likely, and this is confirmed from the Raman analysis. The first two peaks are attributed to the ligands, and the remaining peaks are due to the (120) and (022) planes (JCPDS: 65-1388).

Deconvoluted XPS core level spectra of the main metal node: Cr2p from MIL-53(Cr)-MOF (prepared herein) (Figure 1d) shows two distinct peaks at 589 and 577.4 eV, corresponding to the spin-orbital splitting components of the 2p$_{1/2}$ and 2p$_{3/2}$ of the Cr(III) state. The peak profile matches very well with that reported for Cr2p in a previous report on a MIL-101(Cr)-MOF[39] containing Cr³⁺. The C1s profile (Figure 1e) shows three components at 284.6, 285.1 and 287.9 eV which are attributed to the C-C, C-O and C$_{satellite}$, wherein the C-O bonds arise from the ligand: terephthalic acid. The highly symmetrical O1s signal (Figure 1f) at 531.4 eV corresponds to the Cr-O and the C-O bonds and matches well with a similar signature peak observed for a MIL-101(Cr)-MOF at 531.5 eV in an earlier study[39]. The BET analysis of the Cr-MOF (Figure 1g) reveals it to follow a type IV nitrogen adsorption/desorption isotherm, which represents a mesoporous structure. The surface area of the Cr-MOF is 488 m² g⁻¹ and the average pore diameter is ~2.3 μm. A high effective surface area and a porous structure are most conducive for the adsorption of a large proportion of

the electrolyte ions for redox reactions and for deep electrolyte penetration, thus maximizing the utilization of the available sites for the Faradaic reactions during charge-discharge. The DC-conductivities of pure MIL-53(Cr) and MIL-53(Cr)-BPC composite (containing Cr-MOF:BPC in a weight ratio of 3:1) were determined from I-V plots recorded in a sandwich configuration of SS/sample/SS (SS is stainless steel), over −1 to +1 V (Figure 1h,i). The profiles are mostly linear for the composite and MOF, indicative of an Ohmic dependence, and electrical conductivities (σ) were estimated to be 1.5×10^{-4} and 1.8×10^{-9} S cm^{-1} from the relation: $\sigma = (1/R) \times (d/a)$, where $1/R = \Delta I/\Delta V$ = slope and d and a are the thickness of the sample, and its' area of cross-section. Electrical conduction is poor in the pure MIL-53(Cr) due to the presence of the insulating organic linkers, but conductivity is considerably enhanced by 10^5-orders of magnitude when the MOF is combined with BPC to allow efficient electron movement across its' thickness particularly during cycling. It must be noted that while carbon black is also present in the electrode; it only provides a macroscopic interconnectivity between the active material particles, BPC however, operates at the micro-to-nano-levels.

BPC has micropores and mesopores, and therefore it is able to work at micro-to-nano levels, for it allows deep electrolyte penetration and diffusion, unlike carbon black which does not have this structural advantage. Further unlike carbon black, which is reported to have a low effective surface area in the range of 15-64 m^2 g^{-1}[40], and in contrast, BPC's surface area is 840 m^2 g^{-1}, thus allowing a much higher number of electrochemically accessible sites, thus allowing a high ion-adsorption, and resulting in the observed SC$_{max}$ of 61 F g^{-1} at 0.5 A g^{-1}, obtained via GCD, measured in a BPC/1 M CSA/BPC symmetric supercapacitor (Figure S2).

The electrochemical performance of a BPC//Cr-MOF supercapacitor containing 1 M aqueous CSA as the electrolyte, where Cr-MOF devoid of BPC was used, is shown in Figure S3 (in supporting information) and the cell output (in terms of SC, charge transfer resistance and reversibility) was found to inferior to that of the cell based on the MIL-53(Cr)-BPC composite, thus justifying the use of the composite in this study.

SEM images of MIL-53(Cr) (Figure 2a-c) show the presence of faceted crystals with high dispersity produced by molecular interactions of the organic ligands with the CrO$_6$ octahedra. Elemental analysis for MIL-53(Cr) (Figure 2d) shows distinct peaks from carbon, oxygen and chromium and their atomic percentages were 43%, 33% and 26%, respectively. TEM images of MIL-53(Cr) shows crystals of well-defined shapes of cubes, cuboids and hexagons, approximately, 30-80 nm in dimensions (Figure 2e,f). The high resolution image (Figure 2g) shows lattice fringes, and inter-fringe distances of ~0.34 and ~0.18 nm for the two crystallites, aligning with the (200) and (022) orientations of orthorhombic MIL-53(Cr). The selected area electron diffraction (SAED) pattern with bright spots (Figure 2h), confirms the highly crystalline nature of the Cr-MOF crystals. The spots are assigned to the (120) and (022) planes of orthorhombic chromium oxide.

The XRD pattern of BPC (Figure 3a) exhibits two broad peaks at 2θ = 25.4° (d: 3.5 Å) and 43.2° (d: 2.09 Å), which match with the (002) and (100) planes of hexagonal graphite (JCPDS: 75-1621), albeit, the slightly altered d-spacings, compared to graphite (3.39 and 2.14 Å). BPC's Raman spectrum (inset of Figure 3a) shows the disorder induced D-band at 1348 cm^{-1} which arises due to the structural defects via incorporation of oxygen containing functional groups by alkali functionalization and the G-band at 1595 cm^{-1} produced by the stretching vibrations of the C=C bonds in graphitic materials produces the G-band, characteristic of sp^2 hybridized carbon systems[41]. The 2D or G' band, an overtone of the D-band is also observed at ~2702 cm^{-1}. The I_D/I_G intensity ratio is 1.76, suggesting a high level of functionalization in the material, i.e., presence of −COO, −OH groups, which can potentially increase the cation uptake during electrochemical cycling. The BPC's isotherm (Figure 3b) is a mix of type I and type IV, and the surface area and the average pore diameter are ~840 m^2 g^{-1} and ~2.3 nm respectively. Pore size distribution was also analyzed by the Horvath-Kawazoe method for both MIL-53(Cr) and BPC. For both cases, from this analysis, the pore diameter is less than 1 nm, indicating that micropores are present in the materials, and these pores are beneficial for electrolyte permeation and ion-adsorption. The plots are shown below for ready reference and in the supporting information as Figure S4. The macroporous nature , on the other hand, is reflected in the SEM images shown in Figure (3c-e), where large pores, 3-6 μm in dimensions are seen to be embedded in three dimensional flaky irregular shaped carbon structures.

TEM image (Figure 3f) reveal the contrasting carbon flakes, and the high magnification image (Figure 3g) shows the flakes have a propensity to assemble in the form of overlapping sheets. Lattice fringes are observed only in a few regions and SAED pattern (inset of Figure 3f) shows only diffuse rings, affirming the semi-crystalline nature, in line with the XRD and Raman findings. The I-V behavior of BPC (Figure 3h) exhibits an Ohmic dependence, and the electrical conductivity is calculated to be 5.8×10^{-3} S cm^{-1}. Such a high electrical conductivity permits fast propagation of electrons through the BPC anode matrix, during charge-discharge.

Salient properties of the five liquid electrolytes

The structural formulae of the five electrolytes (in terms of the ionic species and solvent) employed for fabricating independent BPC//MIL-53(Cr) supercapacitor cells are exhibited in Figure 4a. The photographs of the electrolytes, namely: (i) the proton or H$^+$-ion conducting 1 M aqueous CSA solution, the Li$^+$-ion conducting- (ii) 1 M aqueous LiClO$_4$ and (iii) non-aqueous 1 M LiClO$_4$/PC solutions, (iv) [BuMePy]$^+$-ion conducting non aqueous 1 M [BuMePy][CF$_3$SO$_3$]/PC (IL/PC) solution and (v) the Na$^+$-ion conducting aqueous 0.5 (w/v)% NaPSS solution, are shown in Figure 4b. The solutions are clear and either faintly colored or colorless in appearance. The combined effect of the intrinsic properties of the ionic species and the solvent in the electrolyte is reflected in the performance of the BPC//MIL-53(Cr) supercapacitor. High dielectric constant

4

(ε) for efficient salt dissociation, low viscosity for better ion-transport, high boiling point for rendering non-volatility and low freezing point for preventing rapid decline of ionic conductivity (σ_{ionic}) at low temperatures are some of the fundamental prerequisites which the solvent must possess in order to impart high ionic conductivity to the liquid electrolyte. Additional features such as chemical and electrochemical stability and chemical compatibility with the electrodes are also essential[42]. PC and water are high dielectric solvents with ε = 65.1 and 79.8 respectively, thus allowing complete dissociation of the dissolved ionic species. The boiling and freezing points are (241-242 $^{\circ}$C, -48 $^{\circ}$C) and (100 $^{\circ}$C,0 $^{\circ}$C), thus allowing the use of the aqueous electrolytes over a temperature range of 5 to 70 $^{\circ}$C, and the non-aqueous ones over a much wider range. Ionic conductivity is given by: $\sigma = n \times e \times \mu$, where n is the number of free charge carriers or ions, e is the elementary charge, and μ is the ionic mobility. The latter is inversely proportional to the viscosity of the medium (η) via Stokes relation: $\mu = ze/6\pi r\eta$, where r is the radius of the ion.

The variation in viscosity and conductivity of the five electrolytes at 25 $^{\circ}$C are shown in Figure 4c. The viscosity of three aqueous electrolytes (CSA, LiClO$_4$ and NaPSS) are close to unity, 1.3, 0.95 and 1.0 cP respectively. The decline of conductivity is as follows: $\sigma_{NaPSS/water} < \sigma_{LiClO4/PC} < \sigma_{IL/PC} < \sigma_{LiClO4/water} < \sigma_{CSA/water}$. The conductivity of aqueous CSA (267 mS cm^{-1}) electrolyte is greater by an order of magnitude compared to other four electrolytes because of the small size of H$^+$ ion, and possibly because its largely a single ion conductor. The camphorsulfonate anions are comparatively less mobile due to their bulky size, and the protons are free to move in the medium, hopping from one site to another. Although the measure of the mobility index will be lower for the camphorsulfonate anions compared to the protons, but owing to the high conductivity of the medium, they too will migrate towards the positively charged electrode during charge-discharge, under the influence of the applied electric field. This also explains the high SC achieved with the CSA electrolyte.

Ionic radii of Li$^+$ (74 pm), Na$^+$ (116 pm) and ByMePy$^+$ ions are larger compared to H$^+$ (0.87 fm), thus imparting a larger mobility to hydrogen ions. Therefore, the unusually high value of σ_{25} demonstrated by the CSA/H$_2$O solution can be ascribed to: (a) a high dielectric constant, (b) a low viscosity of the solvent and (c) the strong electrostatic interactions that persist between the cationic positive charge and the negative charge on the camphorsulfonate ions as H$^+$ is a hard acid and a strong polarizing ion. The low η and the high ε of water, and the small size of Li$^+$ bestows the LiClO$_4$/water solution with the second highest conductivity. LiClO$_4$/PC has a larger viscosity than IL/PC, imparting a larger conductivity to the latter. NaPSS/water has the lowest conductivity, due to a high effective radius of Na$^+$ ion and low interaction with the anions: PSS. Despite the similarity in terms of anionic group of SO$_3^-$ flanked by the bulky organic species, CSA, and PSS based solutions have the highest and lowest conductivities. The molecular weight of CSA is 232.3 g, and that of NaPSS (weight average) is: M_w =

70000. Its' clear that the water content in the polyelectrolyte will control the ease of ion-movement. The rigid matrix of the polymer inhibits ion-transport, which too lowers ionic conduction.

The conduction behavior of electrolytes are further supplemented by transport numbers, roughly estimated by using Wagner's polarization technique. Figure 4d displays the DC-polarization profiles of the electrolyte soaked separators in a sandwich configuration, with an ion-blocking SS plate on one side, and carbon-fabric(C-fabric)/SS as a non-blocking working electrode (WE) on the other side. The cartoon in the inset of Figure 4d shows the configuration. A constant DC potential of -1 V was applied to the WE for 200 min. during this period the positively charged cation migrates to the WE. At t = 0 s, the initial current is high due to the ionic drift induced by the high concentration of ions in the bulk, and thereafter the current declines exponentially. In the latter region, the current is limited by the diffusion of ions from the bulk solution to the electrode. Subsequently, current almost saturates and acquires a flat plateau like response, because the concentration of ions is depleted in the solution, and at t = 200 min., the current in the cell is basically electronic. I_{total} is the initial current, and $I_{residual}$ is the current at t = 200 min. The transport number of cations (t_{cation} or t_+) is calculated using the following equations.

$$t_{e-} = I_{total}/I_{residual}; \quad t_{cation} \text{ or } t_+ = 1\text{-}t_{e-} \tag{1}$$

Since the total transport number is always unity, $t_+ + t_{e-} = 1$, and the cationic transport number is calculated by subtracting the electronic one from 1. The variation of t_{cation} as a function of electrolyte composition is shown in Figure 4e. The transport number is the highest for LiClO$_4$/water (0.96), closely followed by CSA/water (0.92). NaPSS/water has the lowest transport number, which aligns with the lowest conductivity. A transport number in excess of 0.9 is most advantageous, as it shows that the fraction of the total current carried by H$^+$ ions in CSA/water and Li$^+$ ions in the LiClO$_4$/water dominates ion-transport in these solutions. To further ascertain the stability of the electrolytes over the potential window of operation of the BPC//MIL-53(Cr) supercapacitors, linear sweep voltammograms were also recorded for the electrolytes in the Pt/electrolyte/Pt configuration (Figure 4f). The I-V plots are straight lines, indicating an Ohmic behavior. The overall currents are larger for the CSA/water relative to the other electrolytes, thus implying that ionic conduction is superior for this electrolyte. The superior conductance and transport properties exhibited by the CSA/water electrolyte translates into an enhanced electrochemical performance when used in the BPC//MIL-53(Cr) supercapacitor, in comparison to the performances delivered by the other 4 electrolytes in the same cell.

Since supercapacitors are normally required to operate over a wide temperature range, it is necessary to know how ionic conductivity varies over the operational temperature window of the device. The experimental set-up and the plots of ionic conductivity (σ) as a function of reciprocal absolute temperature are shown in Figure 4g and h. Ionic conductivity was determined from impedance spectra

recorded in a Pt/electrolyte/Pt cell at the open-circuit voltage, over a frequency range of 1 MHz to 1 Hz. Nyquist plots were recorded for each electrolyte over 10 to 70 °C, where individual plots were recorded at intervals of 10 °C. The temperature of the cell was maintained by using a water bath. The cartoon in Figure 4g depicts the cell used for the measurements. The resistance obtained from the first intercept on the abscissa of the Z″ versus Z′ plot was used to calculate the conductivity by employing the relation: $\sigma = 1/R \times (l/a)$, where, l is the distance between the Pt electrodes, and a is the area of cross-section. The thermal dependence indicates an activated process, conductivity increases with increasing temperature, as the ions become more mobile at higher temperatures, due to a lowered viscosity and kinetic energy imparted to the ions. Conductivity varies from 220 to 410 mS cm^{-1} over 10 to 70 °C for the CSA/water electrolyte. The nominal variation in conductivity, and the retention of high conductivity even at low temperature, suggests that Ohmic drop across the BPC//MIL-53(Cr) cell will not be large at low temperatures.

Electrolyte effect on the electrochemical properties of the BPC//MIL-53(Cr) supercapacitor

The ability of the electrolyte to control the electrochemical charge storage performance of the asymmetric BPC//MIL-53(Cr) supercapacitor was confirmed by comparing the specific capacitances obtained from CV and galvanostatic charge-discharge (GCD) plots. Scheme 1 shows the fabrication of the full cell. The CV and GCD plots and the related data are presented in Figure 5. Here CV scans were recorded at different scan rates in the range of 5 to 100 mV s^{-1} over a voltage window of 0 to 1 V for all electrolytes for comparison purpose, and representative CV plots recorded at a scan rate of 5 mV s^{-1} for the BPC//MIL-53(Cr) supercapacitor with the five different electrolytes: 1 M aqueous CSA, 1 M aqueous LiClO₄, 1 M LiClO₄/PC, 1 M IL/PC and aqueous 0.5 (w/v)% NaPSS solutions, are shown in Figure 5a. CV plots were also recorded over a voltage window of 1.5 V, for the BPC//MIL-53(Cr) cells with the non-aqueous electrolytes (IL/PC and LiClO₄/PC) and they are shown in the supporting information (Figure S5). The plots show that with non-aqueous electrolytes, a wider potential window is achievable.

The CV profile for all electrolytes shows a rectangular shape indicating similarity with an ideal supercapacitor behavior. Thus, it can be inferred that the charge storage mechanism for the asymmetric BPC cell follows an electrochemical double layer (EDL) mechanism where positive and negative ions of the electrolytes form a layer at the interface of the respective polarized electrode. Asymmetric supercapacitors with aqueous H$^+$ ion and Li$^+$ ion conducting electrolytes based on CSA and LiClO₄ show the largest enclosed areas, owing to the high ionic conductivity and fast ion-transport exhibited by these solutions. The current density plateaus in the cathodic and anodic branches have larger magnitudes for these cells compared to the remaining three cells, and in particular, the aqueous NaPSS based cell. Representative CV plots for the best and the worst performers, i.e., the BPC/aqueous CSA/MIL-53(Cr) and BPC/aqueous NaPSS/MIL-53(Cr) supercapacitors, as a function of scan

rate, over the operational voltage window of 0 to 1 V are given in Figure 5b and c, and for the remaining electrolytes, they are shown in Figure S6 (supporting information).

For all the BPC//MIL-53(Cr) cells based on the five electrolytes, the enclosed voltammogram areas were found to shrink with increasing scan rate, and since area under the voltammogram is directly proportional to SC, the lower the shrinkage, the better the supercapacitor is. The shrinking is least for the BPC/aqueous CSA/MIL-53(Cr) supercapacitor, thus demonstrating its ability to perform well over fast as well slow charge-discharge rates. The performance comparison was done by quantifying areal capacitance (ASC) by using the following equation, and ASC versus scan rate is illustrated in Figure 5d.

$$ASC\ (mF\ cm^{-2}) = \int [I\ (mA\ cm^{-2}) \times\ dV]/[\nu\ (V\ s^{-1}) \times \Delta V\ (V)] \qquad (2)$$

In (2), I, ν and ΔV are the current, applied scan rate and voltage window respectively. The highest ASCs of 302, 337, 282, 202 and 63 mF cm^{-2} were obtained at a low scan rate of 5 mV s^{-1} for the cells with aqueous CSA, aqueous LiClO₄, LiClO₄/PC, IL/PC and aqueous NaPSS electrolytes. When the scan rate was increased by ten-fold times i.e., 50 mV s^{-1}, ASC retention was obtained as 86, 65, 44, 51 and 71% for the cells based on electrolytes in the aforesaid sequence. At high scan rates (> 20 mV s^{-1}) the performance of the cell with aqueous CSA is greater than that of the cell with aqueous LiClO₄ electrolyte. From the above result, it is deduced that the aqueous CSA electrolyte is the best for the asymmetric BPC//MIL-53(Cr) supercapacitor by considering SC magnitude and SC retention together.

The relatively lower conductivities and the higher viscosities of the non-aqueous electrolytes: LiClO₄ (σ = 7.8 mS cm^{-1}, η = 3.7 cP) and IL (σ = 8.4 mS cm^{-1}, η = 3.0 cP) in PC, compared to the aqueous H$^+$/Li$^+$-ion conducting electrolytes results in a reduced storage response or ASC for the corresponding supercapacitors. However, amongst these two non-aqueous electrolytes, LiClO₄/PC delivers a larger ASC despite the higher viscosity and lower conductivity, possibly due to a greater extent of participation of cations and anions in the double layer formation in comparison to IL/PC where the large size of the cation and the anion restricts the extent of their involvement in the EDL formation. Besides the active role played by the cations, the adsorption of the anion from the electrolyte also governs the supercapacitor performance. Among the anions, the negative charge delocalization can be presumed to follow this order: CSA-with SO₃$^-$ > ClO₄$^-$ ≈ CF₃SO₃$^-$> PSS with SO₃$^-$. Although both CSA, and PSS have the same anionic group, SO₃$^-$, but CSA also has a -C=O bond, thus allows for more delocalization. Camphorsulfonate ion is also less bulkier than the poly(4-styrene sulfonate) anion, and there are no polar groups other than SO₃$^-$ on PSS, thus preventing its' facile adsorption over the active materials, be it BPC or the Cr-MOF. CSA by the virtue of its smaller size and the polar groups, is easily adsorbed across the cross-section of the active materials. Furthermore, on comparing the top performers: aqueous LiClO₄ and CSA, camphorsulfonate is a safer choice than ClO₄$^-$ for the anion[43], and it also allows good negative charge

6

dispersion, thus maximizing ion-dissociation which is reflected in its conductivity.

GCD plots for the asymmetric BPC//MIL-53(Cr) supercapacitor based on the five electrolytes was studied over a current density range of 0.5 to 2.5 A g^{-1}. GCD plots for all the cells irrespective of the electrolyte used (Figure 5e) are triangular, characteristic of charge storage via an EDL mechanism. The SC for the electrodes is calculated using following equation.

$$SC = 2(i * t)/V \qquad (3)$$

In (3), i, t and V are current density (A g^{-1}), discharge time (s) and voltage window (V). GCDs for the best and the least performing supercapacitors containing aqueous CSA and NaPSS respectively, as a function of current density are shown in Figure 5f,g. Maximum SCs of 140, 155, 118, 79 and 20 F g^{-1} are obtained at a current density of 0.5 A g^{-1} for the working electrode, i.e., MIL-53(Cr) in contact with aqueous CSA, aqueous LiClO$_4$, LiClO$_4$/PC, IL/PC and aqueous NaPSS electrolytes respectively. Aqueous CSA and LiClO$_4$ based supercapacitors delivered comparable SCs (Figure 5h) and with increasing current density, the performance differential is lowered. Here, at low current densities, aqueous LiClO$_4$ delivers slightly better performance than aqueous CSA, but the safety feature of the CSA electrolyte makes it ideal. For the remaining electrolytes: SC$_{LiClO4/PC}$ > SC$_{IL/PC}$ > SC$_{NaPSS/H2O}$, which matches with the ASC trend. A comparison chart for MOF based supercapacitors with electrolyte cations similar to the ones used here is plotted in Figure 5i. This includes a Ni$_3$(2,3,6,7,10,11-hexaiminotriphenylene)$_2$ (Ni$_3$(HITP)$_2$) symmetric supercapacitor with a proton conducting electrolyte of tetraethyl ammonium tetrafluoroborate/acetonitrile (TEABF$_4$/ACN) delivered a maximum capacitance of 70 F g^{-1} at 1 A g^{-1} [44]. A symmetrical supercapacitor fabricated with calcined ZIF-8 MOF and containing a 1 M aqueous H$_2$SO$_4$ electrolyte gave a SC of 196 F g^{-1} at 0.1 A g^{-1} [27]. ZIF-67 MOF synthesized from 2-methylimidazole and Co(NO$_3$)$_2$ exhibited a SC of 168 F g^{-1} at 0.5 A g^{-1} by using LiOH electrolyte in three electrode system [45]. In an another study, composite of Mn oxide and calcinated ZIF-8 symmetric supercapacitor delivered 163 F g^{-1} in a 1 M H$_2$SO$_4$ electrolyte [46]. It is obvious that the electrolyte should be chosen carefully by examining the influence of electrolyte type on its intrinsic properties and cell characteristics.

To build a high performance supercapacitor, the iR drop should be minimized as much as possible. The variation of iR drop with current density is given in Figure 6a, and iR drop increases with applied current density. Here the slope is quantitatively equal to $\Delta iR/\Delta I$. Aqueous CSA and LiClO$_4$ electrolytes based supercapacitors show slopes of 0.1 V/A/g and 0.09 V/A/g whereas for the cells based on the remaining electrolytes, it was twice as much: LiClO$_4$/PC (0.2 V/A/g), IL/PC (0.1 V/A/g) and aqueous NaPSS (0.2 V/A/g). A large slope is representative of significant variation in the iR drop, as a function of applied current density. Such a behavior is unacceptable for practical applications. The lower slopes for the aqueous CSA and LiClO$_4$ electrolytes implies good ion and electron transport properties, as reasoned for a supercapacitor containing an ultra-microporous carbon derived from bacterial cellulose [47]. Such a response is ideal

for it represents their suitability for commercial devices. The self-discharge profile for the five electrolytes is presented in Figure 6b. The devices were charged to 1 V by applying 2 mA current and allowed to discharge completely without applying any current. The cells with aqueous CSA, aqueous LiClO$_4$, LiClO$_4$/PC, IL/PC and aqueous NaPSS discharged completely in 12.8, 16.8, 8.0, 4.5 and 2.4 min. respectively. The discharge process is slower for aqueous LiClO$_4$ and CSA electrolytes compared to the cells based on the other three electrolytes. This study also reinforces the practical applicability of the CSA or LiClO$_4$ aqueous electrolytes.

The variation of energy density (E) with power density (P) is displayed in Figure 6c and the values are estimated from the following equations.

$$E(Wh\ kg^{-1}) = C_{cell} \times \frac{\Delta V}{2 \times 3.6} \qquad (4)$$

$$P\ (kW\ kg^{-1}) = \frac{i \times V}{2} \qquad (5).$$

In (4), C_{cell} is half of SC (F g^{-1}) and i is current density (A g^{-1}). Highest energy densities of 9.7, 10.7, 8.2, 5.5 and 1.4 Wh kg^{-1} were achieved for aqueous CSA, aqueous LiClO$_4$, LiClO$_4$/PC, IL/PC and aqueous NaPSS electrolyte based supercapacitors respectively at a power density of 0.25 kW kg^{-1}. When the power density increased by five times (to 1.25 kW kg^{-1}), the retention of energy densities are 81, 74, 41, 42 and 39% for the electrolytes in the above sequence. From the above data it can be concluded that the aqueous CSA electrolyte offers optimal properties for the BPC//MIL-53(Cr) asymmetric supercapacitor. Figure 6d shows the effect of electrolyte on the cycling stability of the asymmetric BPC//MIL-53(Cr) supercapacitors. The variation of SC with number of charge-discharge cycles is shown therein. Supercapacitors with aqueous CSA maintains 85% of capacitance retention after 10,000 cycles whereas for aqueous LiClO$_4$, LiClO$_4$/PC, IL/PC and aqueous NaPSS, the retentions are 90, 80, 80 and 95% respectively.

The electrochemical impedance spectra of the asymmetric BPC//MIL-53(Cr) supercapacitors with aqueous CSA, aqueous LiClO$_4$, LiClO$_4$/PC, IL/PC and aqueous NaPSS electrolytes were recorded over a frequency range of 1 MHz to 0.01 Hz under an AC bias of 20 mV. The ac-potential was superimposed over the respective open-circuit potential during the measurement for each cell. All supercapacitors were tested in their fresh form as well as in their post-cycled states (Figure 6e,f) and fitted into an equivalent circuit, which is shown as an inset of Figure 6e. The data was fitted into a [R(RCPE)] circuit, and the fitted parameters are given in Table 1. Except for the cycled cell with aqueous CSA, all plots encompass a semicircle followed by an inclined straight line. The equivalent series resistance (ESR) values were obtained from the starting point of semicircle on the x-axis or the real part of impedance.

The ESR values are the lowest for the aqueous CSA and LiClO$_4$ electrolytes based supercapacitors and it increased by nearly four-fold times for the cells with the non-aqueous electrolytes of LiClO$_4$ or IL in PC and it increased by ~seven times for the cell with aqueous NaPSS electrolyte. After 10^4 cycles, the ESR values for all the supercapacitors remain in

the same range as that observed for their fresh cells. The medium frequency resistance (R_m) for the aqueous CSA electrolyte based supercapacitor is the lowest (2.7 Ω cm^2), which suggests that charge transfer is very fast due to the low viscosity of the medium, which allows good penetration across the MIL-53(Cr) or BPC electrodes, and also imparts high ionic mobility to the H$^+$ ions, and they easily overcome the resistive barrier at the electrode/electrolyte interface and are injected into the electrode. Aqueous LiClO$_4$, LiClO$_4$/PC, IL/PC and aqueous NaPSS electrolytes based cells exhibit R_{ct} values which are 2-, 30-, 18- and 15- times greater than that of the cell with aqueous CSA. After cycling, R_{ct} values for all supercapacitors increase and maintain similar type trend; only for aqueous LiClO$_4$ based cell, the value is lower than that of the aqueous CSA based cell.

It could be due to an enhanced interaction of the camphorsulfonate ions with the active material, which increases with cycling, and offers an insulating barrier for facile H$^+$ migration. The CPE corresponds to the straight line part of the impedance spectrum, and it is quantified in terms of Y_o and n, through the relation $Z_{CPE} = 1/Y_o(j\omega)^n$. For an ideal supercapacitor: n = 1 and Y_o = C. CPE is therefore a quantified measure of the deviation from an ideal capacitive behavior. The digression from the ideality stems from the high surface roughness of the coated materials as well as the mesh type structure of the Ni foam current collector, which is very different from a regular planar current collector. The electrodes can be visualized to be composed of numerous crests and troughs, and therefore the electrolyte/electrode interface is not smooth and homogenous. A high magnitude of Y_o signifies a high degree of ion-propagation via diffusion across the electrode cross-section. Aqueous CSA based cell shows a larger Y_o compared to the remaining cells, and this differential is maintained even for the post-cycled cells. The net outcome of impedance analysis is as follows: the aqueous CSA electrolyte offers a low resistance for ion-conduction, ion transfer and ion-transport through the bulk of active electrode; processes which control the charge storage performance, and as a consequence its shows an excellent robust electrochemical charge storage response. This is closely followed by the aqueous LiClO$_4$ electrolyte, but safety characteristics of CSA electrolyte are better. In comparison to above two aqueous electrolytes, although the non-aqueous electrolytes show lowered storage performances, but they can be operated over electrochemical potential windows in excess of 1 V. The aqueous NaPSS electrolyte, despite being a polyelectrolyte, is not very suitable for such devices.

Conclusions

The influence of electrolyte type (cation/anion) and the characteristics of the solvent on the electrochemical charge storage performance of an asymmetric BPC//MIL-53(Cr) supercapacitor was studied for the first time by first comparing the electrolyte properties, and then by comparing the redox activities of the cells with the five different electrolytes. The electrolytes considered were: (i) H$^+$ ion conducting aqueous camphorsulfonic acid (CSA), Li$^+$ ion conducting- (ii) aqueous and (iii) non-aqueous LiClO$_4$, (iv) Na$^+$ ion conducting aqueous sodium poly(4-styrene sulfonate) (NaPSS) and (v) ionic liquid (IL:1-butyl-1-methyl-pyrrolidinium trifluoromethanesulfonate). The CSA electrolyte outperformed the studied electrolytes in terms of higher ionic conductivity, larger transport number, ability to carry large currents and maintaining high conductivity even at low temperatures. CSA, is also a quasi-polyelectrolyte, for the anion is neither as compact as conventional salt anions like perchlorate or hydroxide nor is it as bulky as the traditional polyelectrolyte anions like PSS, thus allowing it to be a single-ion conductor, with high mobility, for it is devoid of the rigid polymer matrix that prevails in polyelectrolytes. This effectively translated into an enhanced electrochemical response, for the aqueous CSA based BPC//MIL-53(Cr) supercapacitor showed a SC of 70 F g^{-1}, P_{max} and E_{max} of 9.7 Wh kg^{-1} and 1.25 kW kg^{-1}, and a high cycle life with low capacitance fade. The aqueous LiClO$_4$ based cell also showed a comparable performance, but the low cost, safety aspects, and indigenous local availability renders the aqueous environmentally benign CSA electrolyte to be ideal for practical supercapacitors. The findings of this work can assist immensely in making the right choice for the electrolyte while developing other MOF based supercapacitors.

Supporting information

CV plots of BPC//MIL-53(Cr) supercapacitors with aqueous NaPSS (1.3 V), IL/PC (1.5 V) and LiClO$_4$/PC (1.5 V) and CV recorded over the same voltage window of 0 to 1 V with the following electrolytes: aqueous LiClO$_4$, IL/PC and LiClO$_4$/PC at different sweep rates varying from 5 to 100 mV s^{-1}. This material is available free of charge at http://pubs.acs.org.

Corresponding Author

*Melepurath Deepa

Department of Chemistry, Indian Institute of Technology Hyderabad, Kandi-502285, Sangareddy, Telangana (India).

Email: mdeepa@chy.iith.ac.in, Tel: +91-40-23016252.

References

(1)   Baumann, A. E.; Burns, D. A.; Liu, B.; Thoi, V. S. Metal-Organic Framework Functionalization and Design Strategies for Advanced Electrochemical Energy Storage Devices. *Commun. Chem.* **2019**, *2* (1), 1–14. https://doi.org/10.1038/s42004-019-0184-6.

(2) Xu, G.; Nie, P.; Dou, H.; Ding, B.; Li, L.; Zhang, X. Exploring Metal Organic Frameworks for Energy Storage in Batteries and Supercapacitors. *Mater. Today* **2017**, *20* (4), 191–209. https://doi.org/10.1016/j.mattod.2016.10.003.

(3) Qiu, T.; Liang, Z.; Guo, W.; Tabassum, H.; Gao, S.; Zou, R. Metal–Organic Framework-Based Materials for Energy Conversion and Storage. *ACS Energy Lett.* **2020**, *5* (2), 520–532. https://doi.org/10.1021/acsenergylett.9b02625.

(4) Xie, X.-C.; Huang, K.-J.; Wu, X. Metal–Organic Framework Derived Hollow Materials for Electrochemical Energy Storage. *J. Mater. Chem. A* **2018**, *6* (16), 6754–6771. https://doi.org/10.1039/C8TA00612A.

(5) Yang, J.; Ma, Z.; Gao, W.; Wei, M. Layered Structural Co-Based MOF with Conductive Network Frames as a New Supercapacitor Electrode. *Chem. - Eur. J.* **2017**, *23* (3), 631–636. https://doi.org/10.1002/chem.201604071.

(6) Meng, F.; Fang, Z.; Li, Z.; Xu, W.; Wang, M.; Liu, Y.; Zhang, J.; Wang, W.; Zhao, D.; Guo, X. Porous Co3O4 Materials Prepared by Solid-State Thermolysis of a Novel Co-MOF Crystal and Their Superior Energy Storage Performances for Supercapacitors. *J. Mater. Chem. A* **2013**, *1* (24), 7235–7241. https://doi.org/10.1039/C3TA11054K.

(7) Rajak, R.; Saraf, M.; Mohammad, A.; Mobin, S. M. Design and Construction of a Ferrocene Based Inclined Polycatenated Co-MOF for Supercapacitor and Dye Adsorption Applications. *J. Mater. Chem. A* **2017**, *5* (34), 17998–18011. https://doi.org/10.1039/C7TA03773B.

(8) Li, S.; Yang, K.; Ye, P.; Ma, K.; Zhang, Z.; Huang, Q. Three-Dimensional Porous Carbon/Co3O4 Composites Derived from Graphene/Co-MOF for High Performance Supercapacitor Electrodes. *Appl. Surf. Sci.* **2020**, *503*, 144090. https://doi.org/10.1016/j.apsusc.2019.144090.

(9) Zhang, L. L.; Wei, T.; Wang, W.; Zhao, X. S. Manganese Oxide–Carbon Composite as Supercapacitor Electrode Materials. *Microporous Mesoporous Mater.* **2009**, *123* (1), 260–267. https://doi.org/10.1016/j.micromeso.2009.04.008.

(10) Ragupathy, P.; Park, D. H.; Campet, G.; Vasan, H. N.; Hwang, S.-J.; Choy, J.-H.; Munichandraiah, N. Remarkable Capacity Retention of Nanostructured Manganese Oxide upon Cycling as an Electrode Material for Supercapacitor. *J. Phys. Chem. C* **2009**, *113* (15), 6303–6309. https://doi.org/10.1021/jp811407q.

(11) Yang, Y.; Li, S.; Huang, W.; Shangguan, H.; Engelbrekt, C.; Duan, S.; Ci, L.; Si, P. Effective Synthetic Strategy for Zn0.76Co0.24S Encapsulated in Stabilized N-Doped Carbon Nanoarchitecture towards Ultra-Long-Life Hybrid Supercapacitors. *J. Mater. Chem. A* **2019**, *7* (24), 14670–14680. https://doi.org/10.1039/C9TA03575C.

(12) He, D.; Gao, Y.; Yao, Y.; Wu, L.; Zhang, J.; Huang, Z.-H.; Wang, M.-X. Asymmetric Supercapacitors Based on Hierarchically Nanoporous Carbon and ZnCo2O4 From a Single Biometallic Metal-Organic Frameworks (Zn/Co-MOF). *Front. Chem.* **2020**, *8*. https://doi.org/10.3389/fchem.2020.00719.

(13) Chen, Q.; Li, J.; Liao, C.; Hu, G.; Fu, Y.; Asare, O. K.; Shi, S.; Liu, Z.; Zhou, L.; Mai, L. Ni Foam Supported NiO Nanosheets as High-Performance Free-Standing Electrodes for Hybrid Supercapacitors and Ni–Zn Batteries. *J. Mater. Chem. A* **2018**, *6* (40), 19488–19494. https://doi.org/10.1039/C8TA07574C.

(14) Chen, Y.; Ni, D.; Yang, X.; Liu, C.; Yin, J.; Cai, K. Microwave-Assisted Synthesis of Honeycomblike Hierarchical Spherical Zn-Doped Ni-MOF as a High-Performance Battery-Type Supercapacitor Electrode Material. *Electrochim. Acta* **2018**, *278*, 114–123. https://doi.org/10.1016/j.electacta.2018.05.024.

(15) Rahmanifar, M. S.; Hesari, H.; Noori, A.; Masoomi, M. Y.; Morsali, A.; Mousavi, M. F. A Dual Ni/Co-MOF-Reduced Graphene Oxide Nanocomposite as a High Performance Supercapacitor Electrode Material. *Electrochim. Acta* **2018**, *275*, 76–86. https://doi.org/10.1016/j.electacta.2018.04.130.

(16) Ye, C.; Qin, Q.; Liu, J.; Mao, W.; Yan, J.; Wang, Y.; Cui, J.; Zhang, Q.; Yang, L.; Wu, Y. Coordination Derived Stable Ni–Co MOFs for Foldable All-Solid-State Supercapacitors with High Specific Energy. *J. Mater. Chem. A* **2019**, *7* (9), 4998–5008. https://doi.org/10.1039/C8TA11948A.

(17) Xiao, Z.; Mei, Y.; Yuan, S.; Mei, H.; Xu, B.; Bao, Y.; Fan, L.; Kang, W.; Dai, F.; Wang, R.; Wang, L.; Hu, S.; Sun, D.; Zhou, H.-C. Controlled Hydrolysis of Metal–Organic Frameworks: Hierarchical Ni/Co-Layered Double Hydroxide Microspheres for High-Performance Supercapacitors. *ACS Nano* **2019**, *13* (6), 7024–7030. https://doi.org/10.1021/acsnano.9b02106.

(18) Ding, M.; Cai, X.; Jiang, H.-L. Improving MOF Stability: Approaches and Applications. *Chem. Sci.* **2019**, *10* (44), 10209–10230. https://doi.org/10.1039/C9SC03916C.

(19) Xu, G.; Nie, P.; Dou, H.; Ding, B.; Li, L.; Zhang, X. Exploring Metal Organic Frameworks for Energy Storage in Batteries and Supercapacitors. *Mater. Today* **2017**, *20* (4), 191–209. https://doi.org/10.1016/j.mattod.2016.10.003.

(20) Yu, Z.; Deschamps, J.; Hamon, L.; Karikkethu Prabhakaran, P.; Pré, P. Hydrogen Adsorption and Kinetics in MIL-101(Cr) and Hybrid Activated Carbon-MIL-101(Cr) Materials. *Int. J. Hydrogen Energy* **2017**, *42* (12), 8021–8031. https://doi.org/10.1016/j.ijhydene.2017.02.192.

(21) Ren, J.; Dyosiba, X.; Musyoka, N. M.; Langmi, H. W.; North, B. C.; Mathe, M.; Onyango, M. S. Green Synthesis of Chromium-Based Metal-Organic Framework (Cr-MOF) from Waste Polyethylene Terephthalate (PET) Bottles for Hydrogen Storage Applications. *Int.*

J. Hydrogen Energy **2016**, *41* (40), 18141–18146. https://doi.org/10.1016/j.ijhydene.2016.08.040.

(22) Munusamy, K.; Sethia, G.; Patil, D. V.; Somayajulu Rallapalli, P. B.; Somani, R. S.; Bajaj, H. C. Sorption of Carbon Dioxide, Methane, Nitrogen and Carbon Monoxide on MIL-101(Cr): Volumetric Measurements and Dynamic Adsorption Studies. *Chem. Eng. J.* **2012**, *195–196*, 359–368. https://doi.org/10.1016/j.cej.2012.04.071.

(23) Kayal, S.; Sun, B.; Chakraborty, A. Study of Metal-Organic Framework MIL-101(Cr) for Natural Gas (Methane) Storage and Compare with Other MOFs (Metal-Organic Frameworks). *Energy* **2015**, *91*, 772–781. https://doi.org/10.1016/j.energy.2015.08.096.

(24) Liu, Q.; Ning, L.; Zheng, S.; Tao, M.; Shi, Y.; He, Y. Adsorption of Carbon Dioxide by MIL-101(Cr): Regeneration Conditions and Influence of Flue Gas Contaminants. *Sci. Rep.* **2013**, *3* (1), 2916. https://doi.org/10.1038/srep02916.

(25) Hamon, L.; Serre, C.; Devic, T.; Loiseau, T.; Millange, F.; Férey, G.; Weireld, G. D. Comparative Study of Hydrogen Sulfide Adsorption in the MIL-53(Al, Cr, Fe), MIL-47(V), MIL-100(Cr), and MIL-101(Cr) Metal–Organic Frameworks at Room Temperature. *J. Am. Chem. Soc.* **2009**, *131* (25), 8775–8777. https://doi.org/10.1021/ja901587t.

(26) Serre, C.; Millange, F.; Thouvenot, C.; Noguès, M.; Marsolier, G.; Louër, D.; Férey, G. Very Large Breathing Effect in the First Nanoporous Chromium(III)-Based Solids: MIL-53 or CrIII(OH)·{O2C–C6H4–CO2}·{HO2C–C6H4–CO2H}x·H2 Oy. *J. Am. Chem. Soc.* **2002**, *124* (45), 13519–13526. https://doi.org/10.1021/ja0276974.

(27) Salunkhe, R. R.; Kamachi, Y.; Torad, N. L.; Hwang, S. M.; Sun, Z.; Dou, S. X.; Kim, J. H.; Yamauchi, Y. Fabrication of Symmetric Supercapacitors Based on MOF-Derived Nanoporous Carbons. *J. Mater. Chem. A* **2014**, *2* (46), 19848–19854. https://doi.org/10.1039/C4TA04277H.

(28) Kang, L.; Sun, S.-X.; Kong, L.-B.; Lang, J.-W.; Luo, Y.-C. Investigating Metal-Organic Framework as a New Pseudo-Capacitive Material for Supercapacitors. *Chin. Chem. Lett.* **2014**, *25* (6), 957–961. https://doi.org/10.1016/j.cclet.2014.05.032.

(29) Wang, Y.; Qiao, X.; Zhang, C.; Zhou, X. Development of Structural Supercapacitors with Epoxy Based Adhesive Polymer Electrolyte. *J. Energy Storage* **2019**, *26*, 100968. https://doi.org/10.1016/j.est.2019.100968.

(30) Dou, Q.; Lu, Y.; Su, L.; Zhang, X.; Lei, S.; Bu, X.; Liu, L.; Xiao, D.; Chen, J.; Shi, S.; Yan, X. A Sodium Perchlorate-Based Hybrid Electrolyte with High Salt-to-Water Molar Ratio for Safe 2.5 V Carbon-Based Supercapacitor. *Energy Storage Mater* **2019**, *23*, 603–609. https://doi.org/10.1016/j.ensm.2019.03.016.

(31) Lee, H. Y.; Goodenough, J. B. Supercapacitor Behavior with KCl Electrolyte. *J. Solid State Chem.* **1999**, *144* (1), 220–223. https://doi.org/10.1006/jssc.1998.8128.

(32) Qu, Q. T.; Shi, Y.; Li, L. L.; Guo, W. L.; Wu, Y. P.; Zhang, H. P.; Guan, S. Y.; Holze, R. V2O5·0.6H2O Nanoribbons as Cathode Material for Asymmetric Supercapacitor in K2SO4 Solution. *Electrochem. Commun.* **2009**, *11* (6), 1325–1328. https://doi.org/10.1016/j.elecom.2009.05.003.

(33) Lee, S. J.; Yang, H. M.; Cho, K. G.; Seol, K. H.; Kim, S.; Hong, K.; Lee, K. H. Highly Conductive and Mechanically Robust Nanocomposite Polymer Electrolytes for Solid-State Electrochemical Thin-Film Devices. *Org. Electron.* **2019**, *65*, 426–433. https://doi.org/10.1016/j.orgel.2018.11.044.

(34) Karuppasamy, K.; Vikraman, D.; Hwang, I.-T.; Kim, H.-J.; Nichelson, A.; Bose, R.; Kim, H.-S. Nonaqueous Liquid Electrolytes Based on Novel 1-Ethyl-3-Methylimidazolium Bis (Nonafluorobutane-1-Sulfonyl Imidate) Ionic Liquid for Energy Storage Devices. *J. Mater. Res. Technol.* **2020**, *9* (2), 1251–1260. https://doi.org/10.1016/j.jmrt.2019.11.052.

(35) Pal, B.; Yang, S.; Ramesh, S.; Thangadurai, V.; Jose, R. Electrolyte Selection for Supercapacitive Devices: A Critical Review. *Nanoscale Adv.* **2019**, *1* (10), 3807–3835. https://doi.org/10.1039/C9NA00374F.

(36) Wang, Y.; Kretschmer, K.; Zhang, J.; Kumar Mondal, A.; Guo, X.; Wang, G. Organic Sodium Terephthalate@graphene Hybrid Anode Materials for Sodium-Ion Batteries. *RSC Adv.* **2016**, *6* (62), 57098–57102. https://doi.org/10.1039/C6RA11809G.

(37) Sherif, F. G. Heavy Metal Terephthalates. *Ind. Eng. Chem. Prod. Res. Dev.* **1970**, *9* (3), 408–412. https://doi.org/10.1021/i360035a026.

(38) Linstrom, P. J.; Mallard, W. G. NIST Chemistry WebBook, NIST Standard Reference Database Number 69.

(39) Zhao, M.; Yuan, K.; Wang, Y.; Li, G.; Guo, J.; Gu, L.; Hu, W.; Zhao, H.; Tang, Z. Metal–Organic Frameworks as Selectivity Regulators for Hydrogenation Reactions. *Nature* **2016**, *539* (7627), 76–80. https://doi.org/10.1038/nature19763.

(40) Smith, W. R.; Thornhill, F. S.; Bray, R. I. Surface Area and Properties of Carbon Black. *Ind. Eng. Chem.* **1941**, *33* (10), 5.

(41) Dresselhaus, M. S.; Jorio, A.; Hofmann, M.; Dresselhaus, G.; Saito, R. Perspectives on Carbon Nanotubes and Graphene Raman Spectroscopy. *Nano Lett.* **2010**, *10* (3), 751–758. https://doi.org/10.1021/nl904286r.

(42) Deepa, M.; Sharma, N.; Varshney, P.; Chandra, R.; Agnihotry, S. A. *Ion Conducting Materials: Theory and Applications Edited by AR Kulkarni and P Gopalan*; Narosa Publishing House, New Delhi, 2001. (43)

42. Gray, Fiona Mary ; Connor, J. A. *Polymer Electrolytes.* Cambridge, UK : Royal Society of Chemistry, (RSC Materials Monographs) (1997). 175.

(44) Sheberla, D.; Bachman, J. C.; Elias, J. S.; Sun, C.-J.; Shao-Horn, Y.; Dincă, M. Conductive MOF Electrodes

for Stable Supercapacitors with High Areal Capacitance. *Nat. Mater.* **2017**, *16* (2), 220–224. https://doi.org/10.1038/nmat4766.

(45)   Xia, H.; Zhang, J.; Yang, Z.; Guo, S.; Guo, S.; Xu, Q. 2D MOF Nanoflake-Assembled Spherical Microstructures for Enhanced Supercapacitor and Electrocatalysis Performances. *Nano-Micro Lett.* **2017**, *9* (4), 43. https://doi.org/10.1007/s40820-017-0144-6.

(46)   Yao, M.; Zhao, X.; Jin, L.; Zhao, F.; Zhang, J.; Dong, J.; Zhang, Q. High Energy Density Asymmetric Supercapacitors Based on MOF-Derived Nanoporous Carbon/Manganese Dioxide Hybrids. *Chem. Eng. J.* **2017**, *322*, 582–589. https://doi.org/10.1016/j.cej.2017.04.075.

(47)   Ding, C.; Liu, T.; Yan, X.; Huang, L.; Ryu, S.; Lan, J.; Yu, Y.; Zhong, W.-H.; Yang, X. An Ultra-Microporous Carbon Material Boosting Integrated Capacitance for Cellulose-Based Supercapacitors. *Nano-Micro Lett.* **2020**, *12* (1), 63. https://doi.org/10.1007/s40820-020-0393-7.

Table 1. Fitted parameters of EIS plots for the BPC//MIL-53(Cr) supercapacitors with different electrolytes

Electrolyte	Before cycling			
	ESR (Ω cm^2)	R_{ct} (Ω cm^2)	Y_o (S s^n cm^{-2})	n
Aqueous CSA	1.9	2.7	6.7×10^{-3}	0.60
Aqueous LiClO$_4$	1.5	5	5.0×10^{-3}	0.87
LiClO$_4$/PC	8.7	59	2.8×10^{-3}	0.28
IL/PC	7.7	36	1.5×10^{-3}	0.59
Aqueous NaPSS	14.6	29	8.6×10^{-4}	0.74
After cycling				
Aqueous CSA	1.7	11	5.1×10^{-3}	0.76
Aqueous LiClO$_4$	1.7	7.3	3.6×10^{-3}	0.91
LiClO$_4$/PC	9.2	63	0.9×10^{-3}	0.57
IL/PC	9.0	40.6	2.3×10^{-3}	0.80
Aqueous NaPSS	17.3	39	7.1×10^{-4}	0.84

SCHEME

Scheme 1. Step-wise synthesis of MIL-53(Cr)-MOF and BPC and fabrication of their electrodes and full cell, is shown through photographs and cartoons.
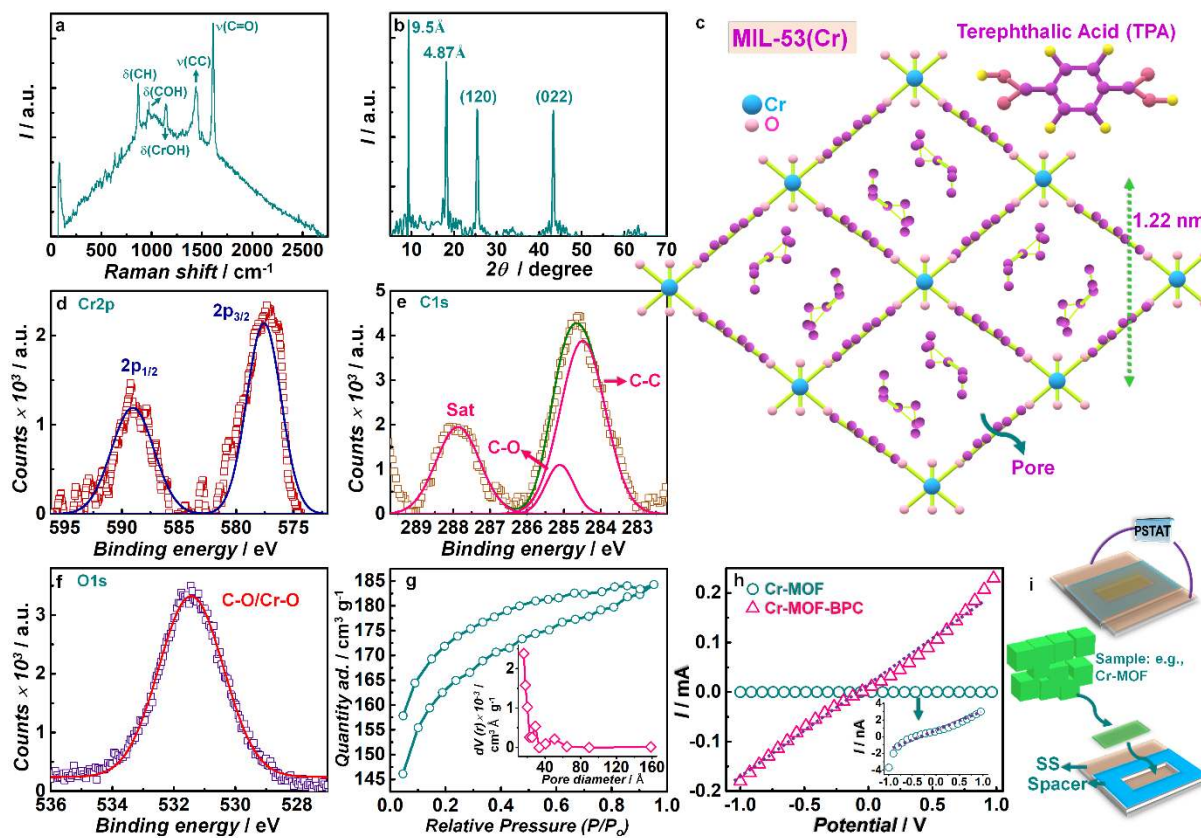
FIGURES

Figure 1. (a) Raman spectrum, (b) XRD pattern and (c) cartoon illustration with the pore-view of Cr-MOF, adapted from[26]. XPS core level spectra of (d) Cr2p, (e) C1s and (f) O1s. (g) Nitrogen adsorption-desorption isotherm (inset shows pore distribution) and (h) I-V characteristics and (i) the cell configuration employed for the measurement.
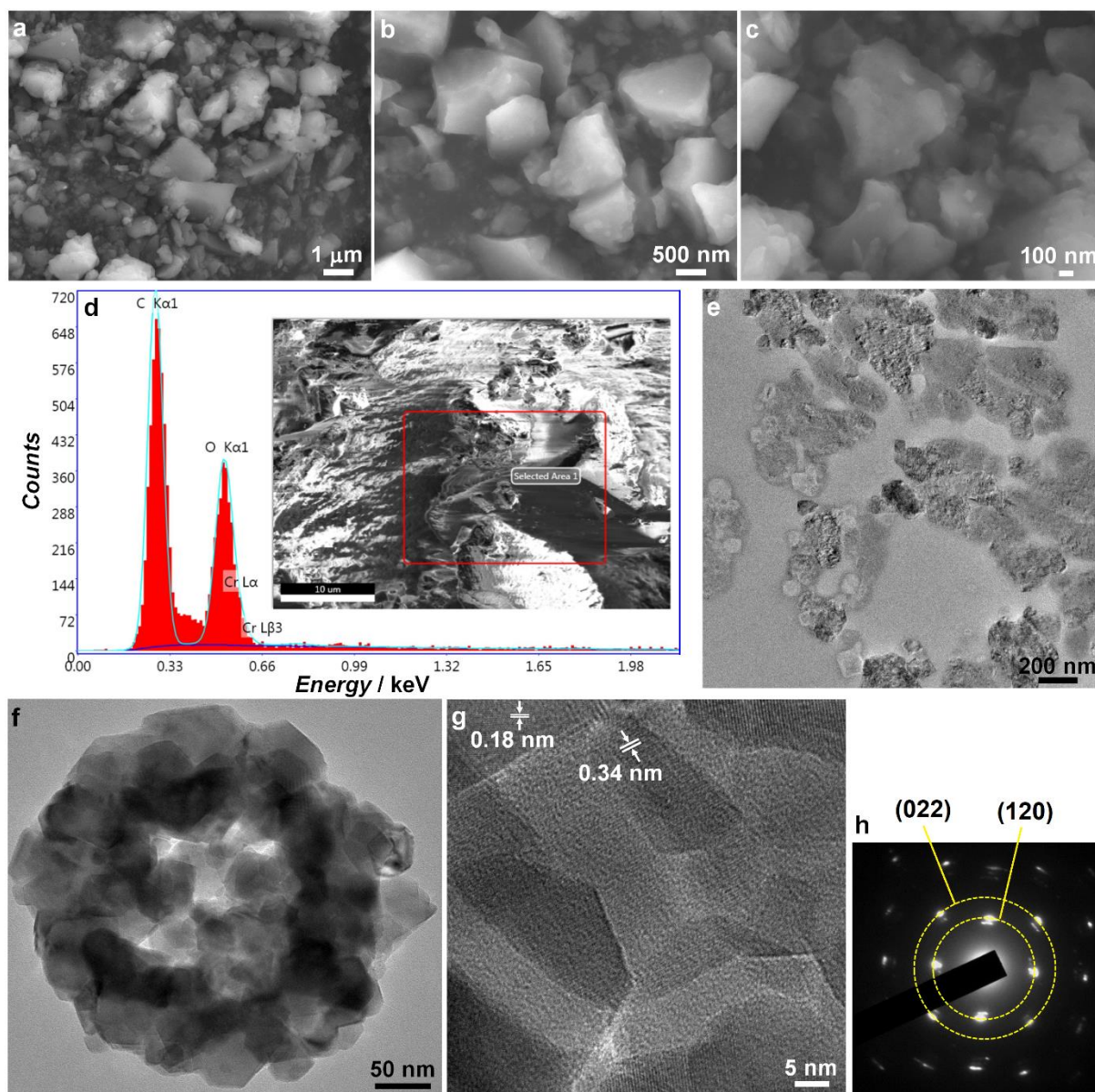
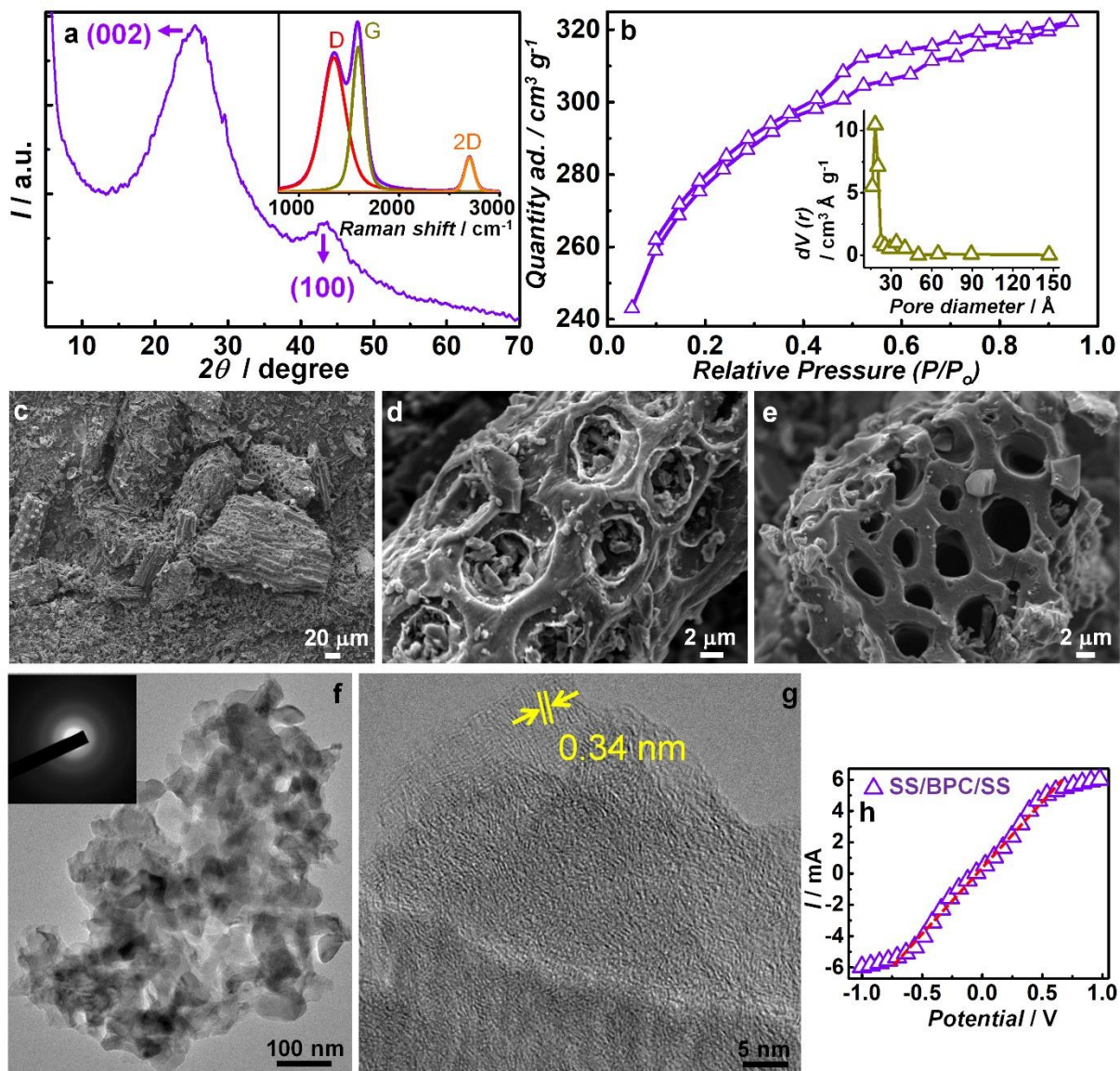**Figure 2.** (a,b,c) SEM images, (d) EDAX analysis, (e,f) TEM images, (g) lattice scale-image and (h) SAED pattern of MIL-53(Cr)-MOF.

Figure 3. (a) XRD pattern (inset show Raman spectrum), (b) nitrogen adsorption-desorption isotherm (inset shows pore distribution), (c-e) SEM images, (f) TEM image (inset is a SAED pattern), (g) lattice-scale images and (h) I-V characteristics of BPC.
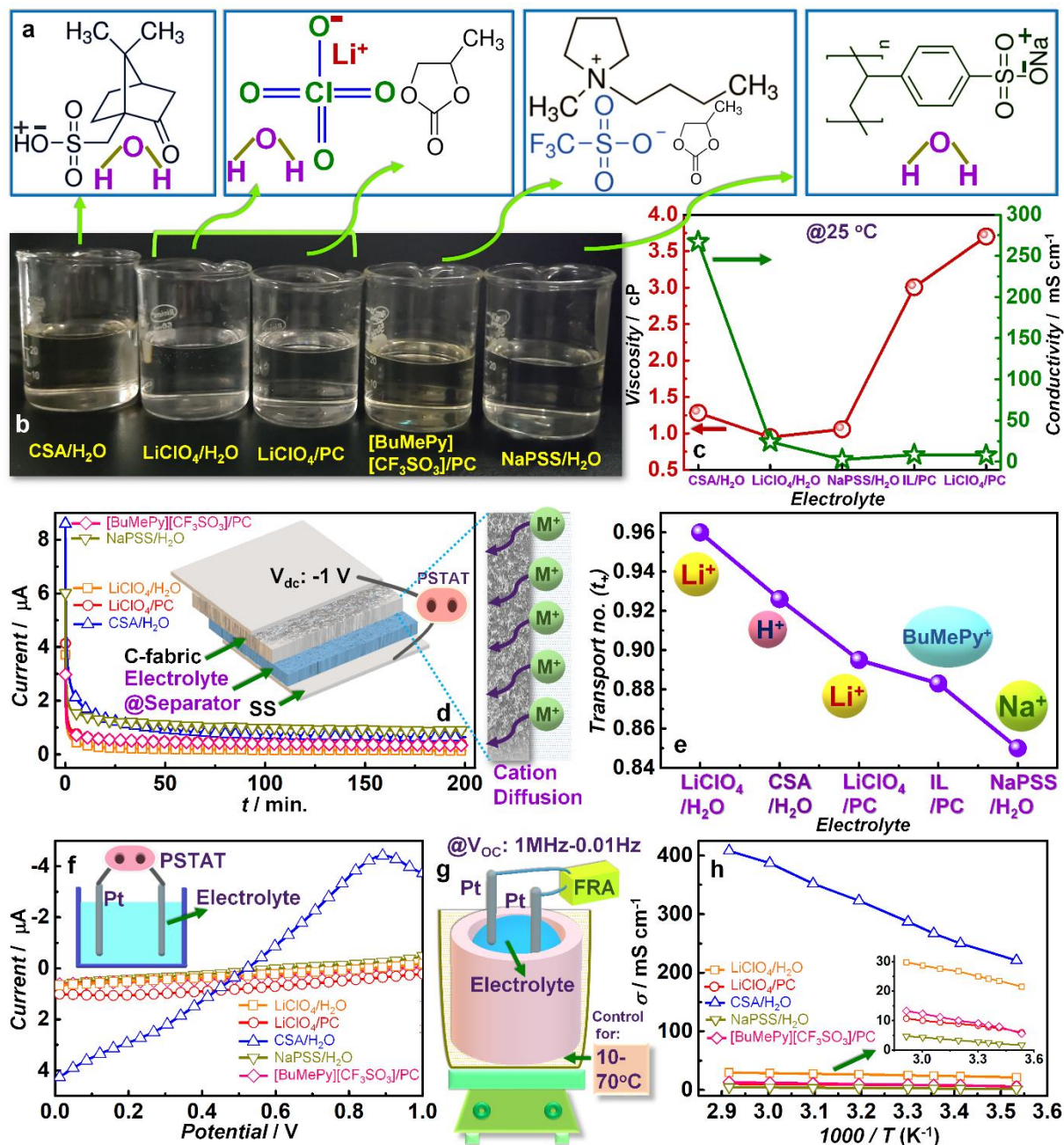
Figure 4. (a) Structural formulae and (b) photographs of the five electrolytes. (c) σ_{25} and η_{25} of the five electrolytes. (d) I versus time transients (inset shows the set-up used for the measurement) and (e) transport number of cations for the five electrolytes. (f) I versus V plots of the five electrolytes (inset shows the experimental set-up) and (g) cartoon showing the cell configuration used for recording-(h) the thermal dependence of conductivity of the electrolytes.
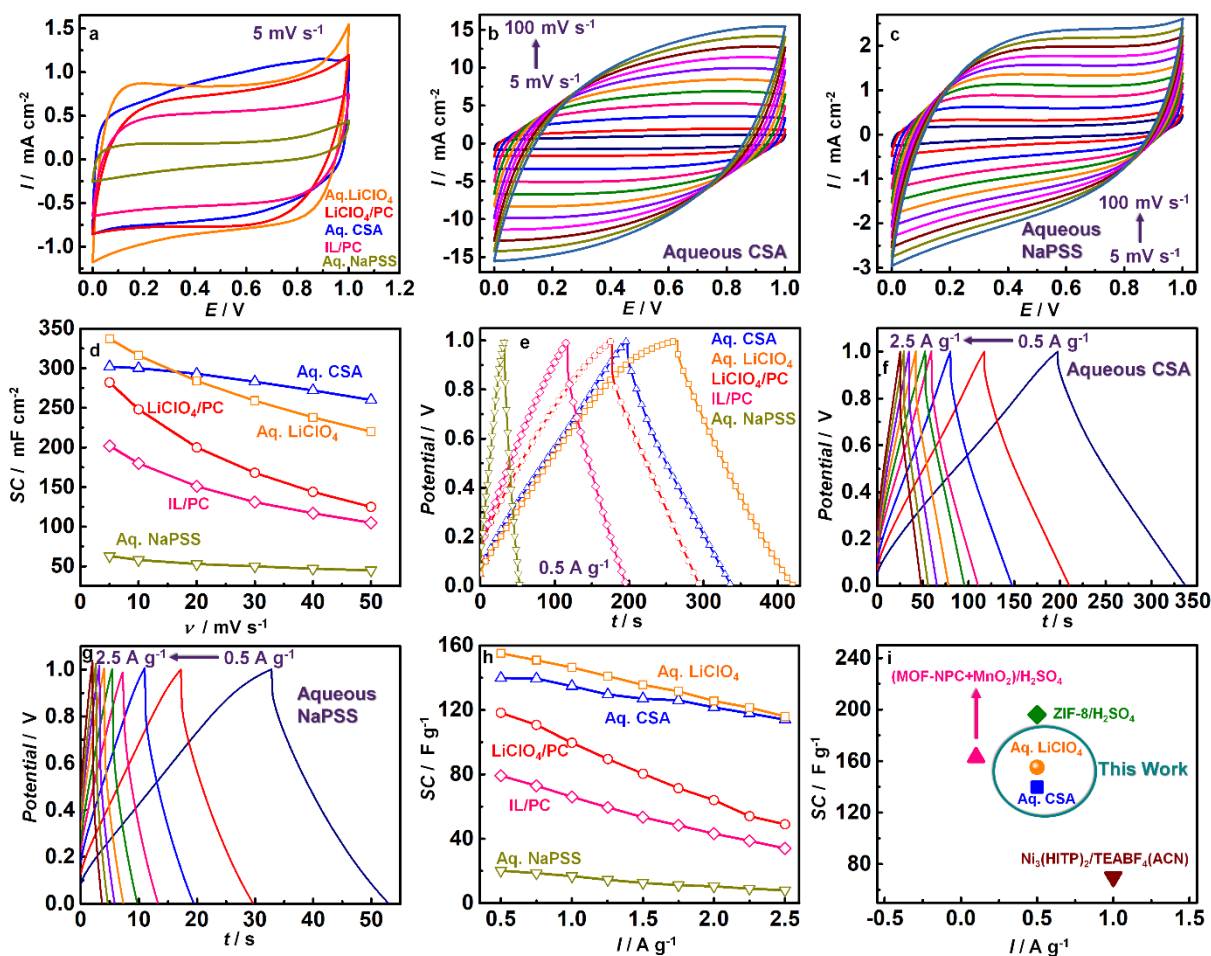
Figure 5. (a) CV plots of asymmetric BPC//MIL-53(Cr) supercapacitors with aqueous CSA, aqueous LiClO₄, LiClO₄/PC, IL/PC and aqueous NaPSS electrolytes at 5 mV s⁻¹. CV plots of (b) BPC/aqueous CSA/MIL-53(Cr) and (c) BPC/aqueous NaPSS/MIL-53(Cr) supercapacitors, as a function of scan rate. (d) ASC variation with scan rate as a function of electrolyte. (e) GCD plots of asymmetric BPC//MIL-53(Cr) supercapacitors with the five electrolytes at 0.5 A g⁻¹. GCD plots of (f) BPC/aqueous CSA/MIL-53(Cr) and (g BPC/aqueous NaPSS/MIL-53(Cr) supercapacitors, as a function of current density. (h) SC variation with current density as a function of electrolyte. (i) Comparison of SCs with literature for MOF based cells with H⁺/Li⁺/ILcation/Na⁺ electrolytes.
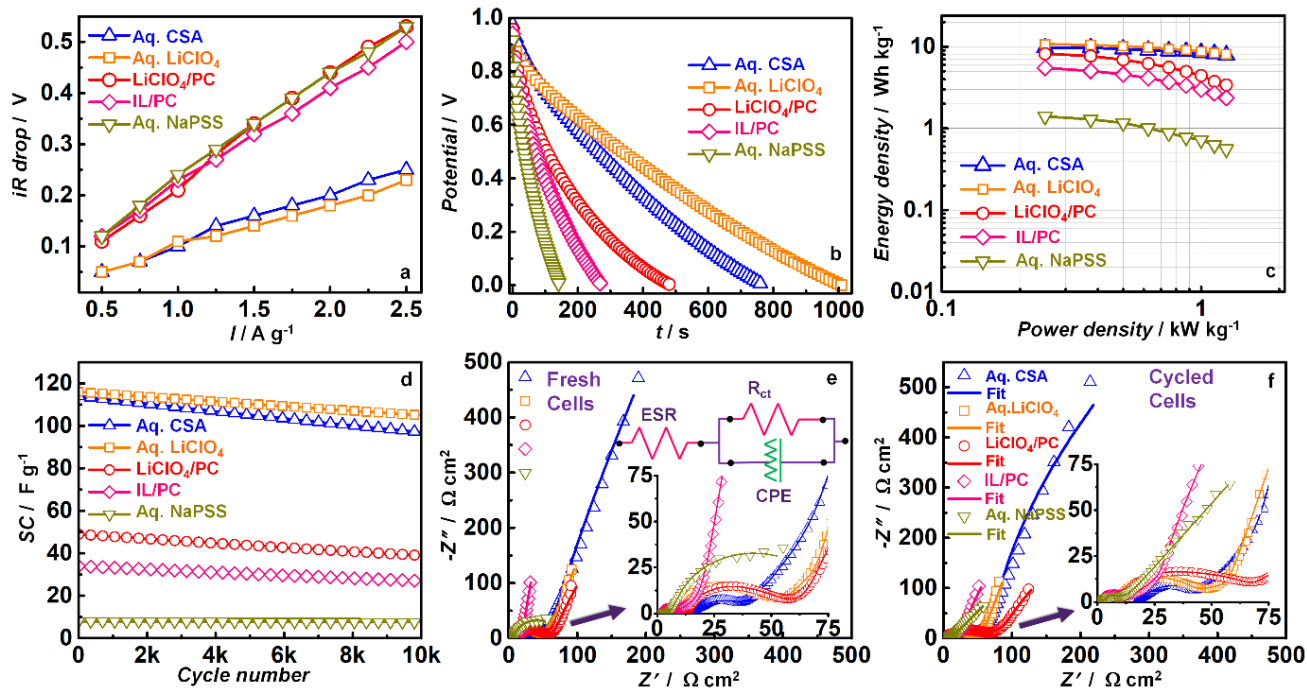
Figure 6. For the asymmetric BPC//MIL-53(Cr) supercapacitors with the five different electrolytes: (a) iR drop- and (b) Self-discharge, (c) Ragone plots of E versus P, (d) SC versus number of charge-discharge cycles and Nyquist plots of (e) fresh and (f) cycled cells, under V_{OC}, and an ac amplitude of 20 mV, over a frequency range of 1 MHz to 0.01 Hz. Inset of (e) shows the equivalent circuit used for fitting the data.